This is a repository copy of *Modelling the impedance response of graded LiFePO4 cathodes for Li-ion batteries*.

White Rose Research Online URL for this paper:
https://eprints.whiterose.ac.uk/209080/

Version: Published Version

The Electrochemical Society
Advancing solid state & electrochemical science & technology

OPEN ACCESS

Modelling the Impedance Response of Graded LiFePO$_4$ Cathodes for Li-Ion Batteries

To cite this article: R. Drummond *et al* 2022 *J. Electrochem. Soc.* **169** 010528

View the underlined article online for updates and enhancements.

Modelling the Impedance Response of Graded LiFePO$_4$ Cathodes for Li-Ion Batteries

R. Drummond,[1,z] C. Cheng,[2] P. S. Grant,[3] and S. R. Duncan[1]

[1]*Department of Engineering Science, University of Oxford, OX1 3PJ Oxford, United Kingdom*
[2]*Warwick Manufacturing Group, University of Warwick, CV4 7AL, Coventry, United Kingdom*
[3]*Department of Materials, University of Oxford, OX1 3PJ Oxford, United Kingdom*

Graded electrodes for Li-ion batteries aim to exploit controlled variations in local electrode microstructure to improve overall battery performance, including reduced degradation rates and increased capacity at high discharge rates. However, the mechanisms by which grading might deliver performance benefit, and under what conditions, are not yet fully understood. A Li-ion battery electrochemical model (a modified Doyle-Fuller-Newman type model capable of generating impedance functions) is developed in which local microstructural changes are captured in order to understand why and when graded electrodes can offer performance benefits. Model predictions are evaluated against experimental electrochemical impedance data obtained from electrodes with micro-scale, controlled variations in microstructure. A region locally enriched with carbon at the electrode/current collector interface is shown to significantly reduce the overpotential distribution across the thickness of a LiFePO$_4$-based Li-ion battery cathode, resulting in a lower charge transfer resistance and impedance. The insights gained from the LiFePO$_4$-based electrodes are generalised to wider design principles for both uniform and graded Li-ion battery electrodes.
© 2022 The Author(s). Published on behalf of ECS by IOP Publishing Limited. [DOI: 10.1149/1945-7111/ac48c6]

Although lithium-ion batteries (LIBs) have established themselves as the principle energy storage technology for mobile electronic devices and electric vehicles, still greater demands are placed on their performance, including further reductions in cost, slower capacity degradation, higher energy/power densities, and improved safety. The usual way to improve battery performance—particularly volumetric and gravimetric capacity—has been to develop novel active material chemistries and to optimize the balance of active material, conductive carbon, binder and porosity in both positive and negative electrodes. New chemistries however can face significant barriers to industrial adoption, including the requirement to "drop in" to existing manufacturing technology and to compete on a cost basis with established LIB chemistries, whose cost continues to fall due to ever growing economies of scale.[1] Consequently, the chemistry of current mass market LIBs is in someways surprisingly similar to that first exploited commercially in the late 1980s, and there remains a lag, or even disconnect, between the materials for LIBs studied in research laboratories and those found in commercial applications. Thus, it may be that many LIB applications will continue to use "traditional" Li-ion chemistries for some time to come.

More recently, attention has started to be given to new ways to engineer existing, proven chemistries into more effective and efficient arrangements within LIB electrodes, as an alternative or as a complement to the development of new active materials and cell chemistries.[2] Critical to this effort is (i) an understanding and quantification of the benefits that microstructural design might bring, and (ii) the development of new manufacturing technologies that allows these designs to be realised in practice.

LIB electrodes are manufactured at the industrial scale by casting a slurry containing the constituent materials (active, carbon conductivity enhancer and polymeric binder) onto a metallic foil current collector that dries to be a random mixture of the materials, and inter-connected pores. Although highly productive and cost effective, there is restricted scope for microstructural design, motivating efforts to develop new electrode formation processes that allow for greater control. At the laboratory scale, through-thickness graded electrodes have been fabricated in a layer-by-layer fashion which allows for controlled through-thickness, local variations in the fraction of the same materials.[3–8] Typically, electrode grading

involves deposition of discrete layers of slightly or radically different formulations to the previous layer, and has been demonstrated for both Li-ion battery[9–11] and supercapacitor[12–14] electrodes, including with near continuous variations in through-thickness microstructure.[15–17] Electrochemical and energy storage benefits of electrode grading have been reported in Ref. 18 where layered, slurry cast LiNi$_{0.5}$Mn$_{1.5}$O$_4$ electrodes provided an 8% reduction in capacity fade over equivalent uniform microstructure electrodes. More recently, LiFePO$_4$-based layer-by-layer graded positive electrodes formed by spray printing exhibited a >120% improvement in degradation rate and a >50% improvement in capacity at 1C compared with equivalent uniform electrodes.[16]

Although some ideas have been postulated, the underlying reasons why certain graded arrangements can deliver improved performance—under certain circumstances—have not fully been elucidated. Without an understanding of which electrode configuration offer benefit—and why—how to design an optimised electrode structure remains obscure. Furthermore, wider acceptance that microstructural control may have value for LIB electrodes will be prevented unless both compelling data and explanations can be provided.

Once spatial variations in microstructure can be allowed in electrode design, such as local fractions of materials, particle size, porosity etc., trial and error exploration becomes an extremely inefficient way to explore the greatly enlarged design space. Moreover, given that somewhat arbitrary grading designs have already shown significant benefits [e.g.[16]], rationally optimised designs can be expected to provide even more compelling benefits; on the other hand, some graded systems may show little improvement over uniform arrangements [e.g. the CA@ designs of Ref. 15].

In this paper, we aim to understand the influence of electrode microstructural grading on the electrochemical response of a LIB positive electrode by modelling the impedance response of graded LiFePO$_4$-based half-cells for which detailed experimental data is already available.[15,16] The paper's main objective is to develop an electrochemical model for the experimental data of Refs. 15, 16 to give confidence that graded electrode designs obtained by optimising with this model sufficiently describe the underlying electrochemical response of the cell. The model is based upon porous electrode theory, being of the Doyle-Fuller-Newman (DFN)-type,[19] but generalised for graded electrodes and generating impedance functions. Focusing on impedance analysis enables the impact of different grading arrangements on the electrochemical behavior to

[z]E-mail: ross.drummond@eng.ox.ac.uk

be unravelled more explicitly than the more common approach of considering only discharge curves. Although LiFePO$_4$ (hereafter termed LFP) is used as the model material (because experimental data is already available), in principle, our approach and insights provided could be applied to similar LIB electrode materials. Previous modelling studies of graded electrodes[5,18,20–28] have principally considered variations in the local electrode porosity, place-to-place via electrode layering, as a means to improve battery energy/power density, generalising previous results that optimised electrode thicknesses and porosities etc.[29–33] But, due to a lack of complementary and flexible manufacturing methods, experimental validation in most studies was generally either somewhat limited, or unavailable.

An electrochemical model that allows analysis of impedance data from Li-ion half-cells consisting of an LFP cathode (positive electrode) and a Li foil anode (negative electrode) is required. Consistent with experiment,[16] the model must allow for local variations in electrode microstructure. LFP is an attractive material for LIBs due to its reasonable energy density ($\approx$170 mAh g^{-1},[34]) low environmental impact (formed from abundant elements,[35]) relatively low Li insertion strain, excellent cycling life (typically thousands of cycles[36]) and good electrochemical stability. However, one of the limitations of LFP is that, compared with most other commercial LIB positive electrode materials, it is relatively insulating with low ionic and electronic conductivity[37] (see later for details). The low conductivity property of the electrodes considered here showing an effective electronic conductivity of $\approx$1 S m^{-1}, suggest that, for large enough current densities, i.e. a charge/discharge rate of $>$1 C, a state of charge inhomogeneity develops so that not all the active LFP across the electrode thickness is utilised in charge storage reactions. We seek to improve this heterogeneous response of the active material by introducing deliberately heterogeneous, graded electrodes with controlled local microstructural variations. In other words, the effect of a spatially varying electrode composition is explored to ameliorate the otherwise inhomogeneous electochemical response of the LFP particles across the electrode thickness.[38–43] In general, it can be expected that grading will have greatest benefit in cases where the ionic and/or electrical transport of the electrode is most challenged i.e. relatively thick ($>$100 μm) electrodes with an active-rich ($>$90 wt%) formulation of intrinsic low conductivity (like LFP) materials, operating under high power requirements ($>$1 C).

In terms of modelling, the LFP-based electrodes are described by a complex system of equation that capture charge and discharge hysteresis,[44,45] inhomogeneous electrode current distributions[38,39,44] and flat open-circuit-potentials. Because interpretation of model data solely from current/voltage data can be challenging,[46] we focus on validating the electrochemical model against more sensitive electrical impedance spectroscopy (EIS) data.[47]

The novel contributions of our approach are: (1) Development of an electrochemical model for Li-ion half-cells that allows for a continuously varying electrode microstructure and an impedance function explicitly linked to the underlying electrochemical equations; (2) Demonstration that electrode grading and, in particular, increasing the local, minority conducting carbon fraction at the current collector significantly reduces the overpotential distribution through the electrode thickness and charge transfer resistance in LFP-based electrodes; (3) Showing that the ratio of electronic to ionic conductivity determines whether active particles discharge first near the current collector or near the separator, i.e. the tendency for heterogeneity of active material utilization; and (4) Proposing that the improved cycle life of graded LFP-based electrodes is due to a reduced fraction of active particles experiencing the most damaging pulverisation.

Notation and definitions

The various spatio-temporal variables used in the LFP-based Li-ion battery model are defined in Table I and the model parameters are described in Tables II and III. The distance across the LFP-based electrode thickness, from current collector toward the separator, is denoted by x, with the electrode/current collector interface at $x = 0$ and the electrode/separator interface at $x = L$. Likewise, r defines the radial distance from the centre of the active spherical LFP particles, with $r = 0$ the particle centre and $r = R_s$ the particle surface.

Experimental Arrangement

Electrodes composed of 80 wt% LiFePO$_4$ active material, 10 wt% carbon black for electronic conductivity enhancement and 10 wt% poly-vinylidenefluoride (PVDF) binder were manufactured using a spray printing approach described in detail in Refs. [15,16]. The basis of the electrode fabrication process is the atomisation of a dilute suspension of the constituents into a spray of suspension droplets that deposit layer-by-layer at a heated current collector mounted on a vacuum chuck, as shown in Fig. 1 available at stacks.iop.org/JES/169/010528/mmedia of the Supplementary Information. The fugitive liquid in the suspension, typically water or isopropyl alcohol, evaporates on the instant of deposition, and by reciprocating the spray over the current collector, the electrode forms incrementally, layer by layer. A critical feature, unavailable in other electrode fabrication processes, is the ability to adjust the composition—or relative fraction of constituents—in each layer, on the fly. For example, consider two suspensions A and B, as illustrated in Fig. 1 of the Supplementary Information. Suspension A was pumped into the spray nozzle by a peristaltic pump and sprayed onto the heated current collector at 140°C. Simultaneously, the composition of suspension A was continuously modified, by the controlled pumping of suspension B into suspension A. For example, suspension B could be relatively concentrated in carbon black so that the resulting electrode will have a progressive through thickness gradient of increasing local carbon black fraction. Such electrodes may have near continuous micron-scale through thickness variations in local proportion of constituents and almost any arbitrary variation can be contrived with a MATLAB code controlling the relative flow rates and concentrations of suspensions A and B.[15]

The through thickness composition gradients, shown schematically in Fig. 2 of the Supplementary Information, were manufactured using LiFePO$_4$ particles (Hydro-Quèbec, Canada), Super-P carbon black (MTI, USA) as the conductivity enhancer and PVDF (poly-vinylidene fluoride, Mw $\sim$ 534,000) as binder, dispersed in NMP (1-Methyl-2-pyrroli-dinone, $\geqslant$99.0%) and IPA (2-propoanol, 99.5%) (all from Sigma-Aldrich, UK). Here, the terminology CAC@ and AC@ is taken from Ref. [15] for consistency. The actual, very similar, sprayed CAC@ and AC@ distributions are shown in detail in Ref. [15].

The various LiFePO$_4$-based cathodes were assembled in CR2032 cells with Li foil and a glass fiber separator soaked in 1M LiPF$_6$ in ethylenecarbonate and dimethyl carbonate (EC/DMC = 50/50 v/v, Sigma-Aldrich, UK) electrolyte. All cell components were stored in a vacuum oven at 60 °C in an Ar filled gloved box for more than 5 hours prior to assembly. The cells were aged for 6–12 h before testing.

Electrochemical impedance spectroscopy was performed using 10 mV sine wave perturbations in the frequency range 1 MHz down to 0.01 Hz after discharging to an open circuit voltage of 2.5 V and ageing of approximately 12 h.

As shown in Fig. 1, the local fraction of materials can be controlled and their variations (depending upon their magnitude) can be expected to also affect the electrode response. Unfortunately, it was not possible to keep the local porosity fraction constant while also varying the local proportion of the electrode materials. To account for this effect, local porosity fraction was measured using cross-sectional microscopy,[16] as shown in Figs. 1a and 1b for the AC@ and CAC@ designs, respectively. Local porosity $\varepsilon(x)$ varied between 0.47 and 0.65 as the LFP fraction varied from 0.9 to 0.55 (with corresponding changes in carbon and binder fraction). The porosity variation followed

Table I. Variables of the electrochemical model.

Variables of the Model

$x \in [0, L]$	Distance across the electrode (m)
$r \in [0, R_s]$	Distance through each particle (m)
$j(\eta(x, t))$	Butler-Volmer kinetics
$\eta(x, t)$	Overpotential (V)
$\phi_s(x, t)$	Solid-phase potential (V)
$\phi_e(x, t)$	Liquid phase potential (V)
$\phi_{el}(x, t)$	Electrode potential
	$\phi_{el}(x, t) = \phi_s(x, t) - \phi_e(x, t)$ (V)
$i_s(x, t)$	Current in carbon/active particle phase (A m^{-2})
$i_e(x, t)$	Ionic current in the electrolyte (A m^{-2})
$I(t)$	Applied current (A).
$i(t)$	Current density. $i(t) = I(t)/S_A$ (A m^{-2})
$v(t)$	Voltage (V)
$c_s(x, r, t)$	Active particle concentration (LiFePO$_4$) (mol m^{-3})
$u_s(x, r, t)$	$u_s(x, t) = rc_s(x, t)$ (mol m^{-2})
$u_s^{surf}(x, t)$	$u_s(x, R_s, t)$ on active particle surface (mol m^{-3}).
$U(u_s^{surf}(x, t))$	Open circuit potential (V)
$c_e(x, t)$	Electrolyte concentration (mol m^{-3})
$w_{AM}(x)$	Weight fraction of active material
$w_{CB}(x)$	Weight fraction of carbon black
$w_{BD}(x)$	Weight fraction of binder
$\Theta(x)$	$\dfrac{a_s(x)}{r_{SEI} + \frac{RT}{i_0}}$
$\Gamma(x)$	$\left(\dfrac{1}{\sigma(x)} + \dfrac{1}{\kappa(x)}\right)^{-1}$ (S m^{-1})
$\Sigma(x)$	$\left(1 + \dfrac{\sigma(x)}{\kappa(x)}\right)^{-1}$
$\varepsilon(x)$	Local porosity
$v_{vol}(x)$	Volume fraction of LiFePO$_4$ active material
$a_s(x)$	Specific interfacial area (m^2/m^3)

$$\varepsilon_{data}(x) = 1 - \frac{W(w_{AM}, w_{CB}, w_{BD})}{V}$$
$$\times \left(\frac{w_{AM}}{\rho_{AM}} + \frac{w_{CB}}{\rho_{CB}} + \frac{w_{BD}}{\rho_{BD}}\right), \quad [1]$$

where $W(w_{AM}, w_{CB}, w_{BD})$ is the electrode weight (itself being a function of the electrode composition), V the electrode volume (so $W(w_{AM}, w_{CB}, w_{BD})/V$ is the electrode density), w_{AM} is the mass fraction of active material having density ρ_{AM}, w_{CB} is the mass fraction of carbon black with density ρ_{CB} and w_{BD} is the mass fraction of PVDF binder with density ρ_{BD}, with the weight fractions linked by $w_{AM} + w_{CB} + w_{BD} = 1$. The complex dependency between local electrode composition and porosity captured in Eq. 1 was incorporated into the model in a linear form using weights θ_{AM}, θ_{CB}, and θ_{BD} to represent the different porosity contribution according to:

$$\varepsilon(x) = \theta_{AM} w_{AM}(x) + \theta_{CB} w_{CB}(x)$$
$$+ \theta_{BD} w_{BD}(x) + \theta_{const}. \quad [2]$$

Linear regression to the porosity data gave best-fit values of $\theta_{AM} = -0.5066$, $\theta_{CB} = 0.0962$, $\theta_{BD} = 0.0377$ and $\theta_{const} = 0.9205$, with the best-fit variations also shown in Fig. 1.

The Electrochemical Model

The electrochemical model is introduced to produce the impedance response of the different electrodes, suitable for comparison with experiment. The model is posed within the classic framework of the Newman group (e.g.[19,48,49]) and observes the standard

assumptions of that approach, such as electrode homogenisation and the use of a pseduo-2D domain Ref. 50. The novelty of the model is the ability to describe electrodes with continuously varying local proportions of active material, carbon black and binder through the thickness, and the way in which an impedance function is generated from the electrochemical equations.

Dependence of model parameters on local electrode composition.—Prior to introducing the model equations, a relationship between the local electrode composition, defined by the weight fraction of active material $w_{AM}(x)$, carbon black $w_{CB}(x)$ and binder $w_{BD}(x)$, and the model parameters, in particular $D_e(x)$, $\sigma(x)$, $\kappa(x)$ and $a_s(x)$,[51,52] must be established. The weight fractions are the controlled variable of the spray deposition process and may take values between [0, 1], for example with $w_{AM}(x) = 0$ a region with no active particles and $w_{AM}(x) = 1$ a region entirely of active particles. Parameters $D_e(x)$, $\sigma(x)$, $\kappa(x)$ and $a_s(x)$ were then obtained using Bruggeman-type relationships, as used in Refs. 53–56 for example, based on the local porosity $\varepsilon(x)$ and the carbon black weight fraction $w_{CB}(x)$. Thus, the ionic conductivity was given by

$$\kappa(x) = \kappa_\infty \varepsilon(x)^{b_\kappa}, \quad [3]$$

and the electrolyte diffusivity by

$$D_e^{eff}(x) = D_e \varepsilon(x)^{b_{D_e}}. \quad [4]$$

From experimental data,[15] the local electronic conductivity was related to the local weight fraction of carbon black by

$$\sigma(x) = \sigma_\infty w_{CB}(x)^{b_\sigma}. \quad [5]$$

Figure 2 shows a plot of electronic conductivity with fraction of carbon black according to Eq. 5, with a good fit to the data for electrodes made with controlled carbon content.

The local weight fraction of active material will also affect the local reacting surface area $a_s(x)$. Assuming spherical particles, this area can be approximated[57] by

$$a_s(x) = \frac{3v_{vol}(x)}{R_s} \approx \frac{3(1 - \varepsilon(x))}{R_s} \quad [6]$$

where $v_{vol}(x)$ is the local volume fraction of active material.

Current flow.—The following set of equations from the DFN model define the current through the electrode

$$a_s(x)C^{sp}\frac{\partial\phi_{el}(x, t)}{\partial t} = \frac{\partial i_e(x, t)}{\partial x} - a_s(x)Fj(x, t), \quad [7]$$

$$i_e(x, t) = -\kappa(x)\frac{\partial\phi_e(x, t)}{\partial x}, \quad [8]$$

$$i_s(x, t) = -\sigma(x)\frac{\partial\phi_s(x, t)}{\partial x}, \quad [9]$$

$$i(t) = i_s(x, t) + i_e(x, t). \quad [10]$$

Equation 7 is the divergence equation adapted with a double layer term,[58,59] Eq. 8 is MacInnes' equation without bulk electrolyte effects, Eq. 9 is Ohm's law for the solid phase current, and Eq. 10 is Kirchhoff's law for current conservation for ionic and electronic currents.

The system described by Eqs. 7–10 is driven by the applied current density $i(t)$ and the active particle/electrolyte inter-facial reaction rate $j(x, t)$, which governs the rate of Li intercalation into the LFP particles. Within the DFN model framework, this rate is described by Butler-Volmer kinetics

Table II. Electrochemical model parameters.

	Electrochemical Parameters		
Symbol	Definition	Value	Units
σ_∞	Free electronic conductivity	4.01	S m^{-1}
b_σ	Bruggeman coefficient	1.7	
κ_∞	Free ionic conductivity	2.6	S m^{-1}
b_κ	Bruggeman coefficient	1.5	
D_e	Bulk ionic diffusivity	8×10^{-8}	m^2 s^{-1}
b_{D_e}	Bruggeman coefficient	1.5	
D_e^{sep}	Separator ionic diffusivity	8×10^{-8}	m^2 s^{-1}
L	Cathode length	110×10^{-6}	m
C^{sp}	Double layer capacitance	0.067	F
D_s^{de}	Li-deficient diffusion coef.	7.3×10^{-18}	m^2 s^{-1}
D_s^{ri}	Li-rich diffusion coef.	9×10^{-15}	m^2 s^{-1}
R	Universal gas constant	8.3140	J K^{-1} mol^{-1}
F	Faraday's constant	96 487	C mol^{-1}
T	Temperature	297	K
t_+	Transference number	0.22	
S	Electrode surface area	1.131×10^{-4}	m^2
n	# discretisation elements	30	
R_s	Active particle radius	900×10^{-9}	m
R_s^{ri}	Radius of inner core region	λR_s	m
λ	R_s^{ri}/R_s	0.9	
c_e^*	Equilibrium electrolyte conc.	10^3	mol m^{-3}
$dU(u_s^{surf})/du_s^{surf}$	Open circuit potential slope	Table III	V m^2 mol^{-1}
R_{res}	Resistance	Table III	Ω
r_{SEI}	Film resistance	Table III	Ω m^2
i_0	Ion exchange current density	Table III	A m^{-2}

Table III. Model parameters that vary for each electrode composition.

	Electrochemical			SEI		Anode		
Variable	$\dfrac{1}{r_{SEI} + \frac{RT}{Fi_0}}$	R_{res}	$dU(.)/du_s^{surf}$	C_{SEI}	R_{SEI}	C_{con}	R_{con}	C_{foil}
AC@	3.90	4.52	6.39×10^4	1.80×10^{-5}	8.95	6.67×10^{-5}	1.40	1.11
CAC@	1.90	4.52	5.64×10^4	1.47×10^{-5}	10.96	6.67×10^{-5}	1.50	1.14
Uniform	0.69	5.90	3.96×10^4	2.55×10^{-5}	48.90	5.0×10^{-5}	2.0	1.28
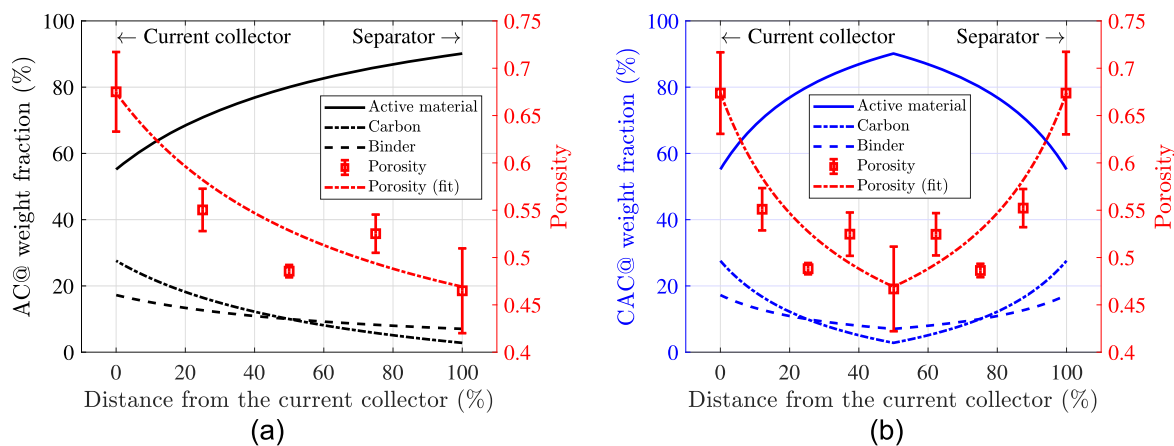
Figure 1. Variation in the local porosity fraction and electrode composition through the LiFePO$_4$-based electrode thickness for the AC@ and CAC@ electrodes designs taken from Ref. 16 (a) Electrode porosity and variation in composition through the electrode thickness for the AC@ design of Ref. 16 and the best-fit of the porosity fraction to Eq. 2. (b) Electrode porosity and variation in composition through the electrode thickness for the CAC@ design of Ref. 16 and the best-fit of the porosity fraction to Eq. 2.
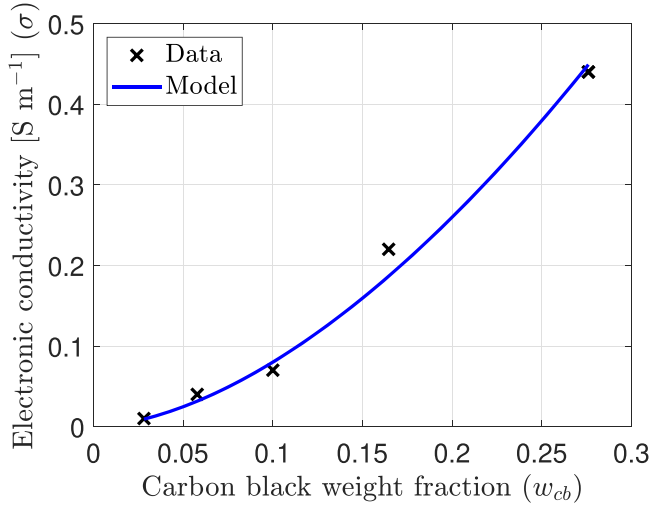
Figure 2. Dependency of the electronic conductivity (σ) on the weight fraction of carbon black for the LFP-based cathode. The model followed $\sigma = \sigma_\infty w_{CB}^{b_\sigma}$ with the data obtained from Ref. 15.

$$j(\eta(x, t)) = \frac{i_0}{F} \sinh\left(\frac{F}{RT}\eta(x, t) - r_{SEI}Fj(\eta(x))\right), \quad [11]$$

where r_{SEI} is the thickness of the solid-electrolyte interface (SEI) and the local overpotential $\eta(x, t)$ is

$$\eta(x, t) = \phi_s(x, t) - \phi_e(x, t) - U(u_s^{surf}(x, t)). \quad [12]$$

The ion exchange current density $i_0(x)$ is assumed to be constant under the small signal assumption of impedance. For the impedance analysis, the nonlinear Butler-Volmer reaction kinetics of Eq. 11 is also linearised around $\eta(x) = 0$

$$Fa_s(x)j(\eta(x, t)) \approx \left(\frac{a_s(x)}{r_{SEI} + \frac{RT}{Fi_0}}\right)\eta(x, t)$$
$$= \Theta(x)\eta(x, t). \quad [13]$$

The model boundary conditions at the current collector are such that all of the current is carried by electrons in the solid "matrix", consisting of the active particles and carbon, with $i_s(0, t) = i(t)$, $i_e(0, t) = 0$, while at the separator boundary, all of the current is carried by ions in the liquid electrolyte with $i_e(L, t) = i(t)$, $i_s(L, t) = 0$.

The voltage drop across the electrode is given by

$$v(t) = v_\phi(t) + v_{contact}(t) + v_{anode}(t)$$
$$+ v_{c_e}(t) + R_{res}i(t) \quad [14]$$

where $v_\phi(t)$ is the potential difference between the active particles at the current collector and the electrolyte at the separator, which accounts for the charge transfer resistance and the potential drop from ions diffusing within the active particles, $v_{contact}(t)$ is the voltage drop from the contact resistance at the current collector/cathode interface,[60] $v_{c_e}(t)$ is the potential induced by the bulk electrolyte concentration buildup and $v_{anode}(t)$ is caused by the voltage drop across the solid-electrolyte interface (SEI) at the anode.[46]

Overpotential Dynamics.—Overpotential relaxation dynamics are now introduced to define the charge transfer resistance, which is the resistance that must be overcome to transport charge carried by an electron at the current collector to an ion at the separator. Following Ref. 59, the ionic current is first expressed as

$$i_e(x, t) = i(t) - i_s(x, t) = \sigma(x)\frac{\partial\phi_s(x, t)}{\partial x} + i(t)$$
$$= \Gamma(x)\frac{\partial\phi_{el}(x, t)}{\partial x} + \Sigma(x)i(t),$$

where $\phi_{el} = \phi_s - \phi_e$ is the electrode potential, $1/\Gamma(x) = 1/\sigma(x) + 1/\kappa(x)$ and $\Sigma(x) = \kappa(x)/(\sigma(x) + \kappa(x))$. Note that if $\sigma \ll \kappa$, as is often the case for LFP cells[44] then $\Gamma(x) \approx \sigma(x)$ and $\Sigma(x) \approx 1$. Differentiating the above expression in space (under the assumption that the spatially varying electrode composition is a differentiable function—if it is not, then the modelling approaches of studies such as Refs. 12, 17 for layered electrodes can be applied)—gives the ionic current flux

$$\frac{\partial i_e(x, t)}{\partial x} = \frac{\partial}{\partial x}\left(\Gamma(x)\frac{\partial\phi_{el}(x, t)}{\partial x}\right) + \frac{d\Sigma(x)}{dx}i(t). \quad [15]$$

Substituting Eq. 15 back into the capacitive equation Eq. 7 gives

$$a_s(x)C^{sp}\frac{\partial\phi_{el}(x, t)}{\partial t} = \frac{\partial}{\partial x}\left(\Gamma(x)\frac{\partial\phi_{el}(x, t)}{\partial x}\right)$$
$$+ \frac{\partial\Sigma(x)}{\partial x}i(t) - a_s(x)Fj(\eta(x, t)) \quad [16]$$

Equation 16 is not yet in a state-space form from which it is possible to derive an impedance, as ϕ_{el} and η have different equilibria. This is addressed by converting Eq. 16 into a model for the overpotential dynamics by assuming that the slope of the open circuit potential (OCP) $U(u_s^{surf})$ with respect to the particle surface concentration (c_s^{surf}) is small. As the OCP of LFP is generally flat,[61] this assumption generally holds, and Eq. 12 implies that variations in the electrode potential are approximately the same as the overpotential $\partial\phi_{el}(x, t) \approx \partial\eta(x, t)$, so

$$a_s(x)C^{sp}\frac{\partial\eta(x, t)}{\partial t} = \frac{\partial}{\partial x}\left(\Gamma(x)\frac{\partial\eta(x, t)}{\partial x}\right)$$
$$+ \frac{d\Sigma(x)}{dx}i(t) - a_s(x)Fj(\eta(x, t)). \quad [17]$$

For small-signal impedance analysis, the nonlinearity of $j(\cdot)$ in Eq. 17 can be linearised around $\eta = 0$, as in Eq. 13, to give the spatially heterogeneous semi-linear convection-reaction-diffusion equation

$$a_s(x)C^{sp}\frac{\partial\eta(x, t)}{\partial t} = \frac{\partial}{\partial x}\left(\Gamma(x)\frac{\partial\eta(x, t)}{\partial x}\right)$$
$$+ \frac{d\Sigma(x)}{dx}i(t) - \theta(x)\eta(x, t). \quad [18]$$

The equivalent dynamics for uniform electrodes are

$$a_s C^{sp}\frac{\partial\eta(x, t)}{\partial t} = \Gamma\frac{\partial^2\eta(x, t)}{\partial^2 x} - \frac{i_0 a_s F}{RT}\eta(x, t), \quad [19]$$

which is a reaction-diffusion equation with an analytical solution.[58] No such analytical solution could be found for Eq. 18 with generic spatially varying coefficients.

Under the flat OCP assumption, the boundary conditions for the overpotential $\eta(x, t)$ at the current collector are

$$\frac{\partial\eta(x, t)}{\partial x}\Big|_{x=0} = -\frac{i(t)}{\sigma(0)}, \quad [20]$$

and at the separator are

$$\frac{\partial\eta(x, t)}{\partial x}\Big|_{x=L} = \frac{i(t)}{\kappa(L)}. \quad [21]$$

The relaxation of the double layer, as in the dynamics of η, is significantly faster than the other electrochemical phenomena of the model, such as (de)intercalation. This time-scale separation can be exploited to decouple the various electrochemical effects in the impedance response and simplify the analysis. Specifically, the equilibrium overpotential $\eta^*(x)$ is defined as the solution to

$$0 = \frac{d}{dx}\left(\Gamma(x)\frac{d\eta^*(x)}{dx}\right) + \frac{d\Sigma(x)}{dx}i(t) - \theta(x)\eta^*(x) \quad [22]$$

where $\eta^*(x)$ is subject to the boundary conditions of Eqs. 20–21. The spatially varying equilibrium reactivity $j(\eta^*(x))$ can then be computed exactly and fed into the active particle and electrolyte dynamics described above.

To define an impedance function for the porous electrode, the voltage drop across the electrode $v_\phi = \phi_s(0, t) - \phi_e(L, t)$ (as in the potential difference between the solid phase at the current collector minus the liquid phase at the separator) must be defined. This voltage drop can be written as a path integral

$$v_\phi(t) = \phi_s(0, t) - \phi_e(L, t), \quad [23]$$

$$= \phi_{el}(0, t) + \phi_e(0, t) - \phi_e(L, t), \quad [24]$$

$$= \phi_{el}(0, t) - \int_0^L \frac{\partial\phi_e(x, t)}{\partial x}dx. \quad [25]$$

By re-writing the electrolyte potential gradient Eq. 8 as

$$-\frac{\partial\phi_e(x, t)}{\partial x} = \frac{i_e(x, t)}{\kappa(x)} = \left(\frac{\sigma(x)}{\sigma(x) + \kappa(x)}\right)$$
$$\times \frac{\partial\phi_{el}(x, t)}{\partial x} + \frac{i(t)}{\sigma(x) + \kappa(x)}, \quad [26]$$

and using Eq. 12, then $v_\phi(t)$ can be written in terms of the overpotential and the open circuit potential (two of the model's states)

$$-v_\phi(t) = \eta(0, t) + U(c_s^{surf}(0, t))$$
$$+ \int_0^L \frac{i(t)}{\sigma(x) + \kappa(x)}dx$$
$$+ \int_0^L \left(\frac{\sigma(x)}{\sigma(x) + \kappa(x)}\right)$$
$$\times \left(\frac{\partial\eta(x, t)}{\partial x} + \frac{\partial U(c_s^{surf}(x, t))}{\partial x}\right)dx, \quad [27]$$

with the integrals evaluated numerically in the model using the midpoint rule.

Ion diffusion in the active material particles.—Ion diffusion within the active particles is included in the model in order to capture the low frequency tail of the impedance plot. LFP particle electrochemical dynamics are complicated by the phase transformations that take place during intercalation[44] and the resulting hysteresis (having a different response upon charging and discharging). For instance, it was proposed in Ref. 44 to model LFP particles as developing a lithium-rich core surrounded by a Li deficient outer region. The standard approach to model this multi-phase system is to introduce a moving boundary at the interface between the two regions,[44] but here it is assumed that the small signals of impedance allow the assumption this boundary remains fixed (and in reality it is of course a diffuse boundary), and, instead, each region diffuses separately, but are connected by a constant flux boundary condition.

Assuming spherical particles and defining the radius of the inner core region as $R_s^{ri} = \lambda R_s$ and furthermore $u_{s,r}^{de}(x, r, t) = rc_s^{de}(x, r, t)$

and $u_s^{ri}(x, r, t) = rc_s^{ri}(x, r, t)$ as the scaled concentrations in the lithium rich and deficient regions, then, within each particle region, the ions are assumed to diffuse according to

$$\frac{\partial u_s^{ri}(x, r, t)}{\partial t} = D_s^{ri}\frac{\partial^2 u_s^{ri}(x, r, t)}{\partial r^2}, \quad \forall r \in (0, R_s^{ri}), \quad [28]$$

$$\frac{\partial u_s^{de}(x, r, t)}{\partial t} = D_s^{de}\frac{\partial^2 u_s^{de}(x, r, t)}{\partial r^2}, \quad \forall r \in (R_s^{ri}, R_s), \quad [29]$$

and be subject to the boundary conditions $u_s^{ri}(x, 0, t) = 0$, $u_s^{ri}(x, R_s^{ri}, t) = u_s^{de}(x, R_s^{ri}, t)$,

$$D_s^{ri}\frac{\partial}{\partial r}\left(\frac{u_s^{ri}(x, r, t)}{r}\right)\bigg|_{r=R_s^{ri}}$$
$$= D_s^{de}\frac{\partial}{\partial r}\left(\frac{u_s^{de}(x, r, t)}{r}\right)\bigg|_{r=R_s^{ri}}, \quad [30]$$

$$\frac{1}{R_s}\frac{\partial u_s^{de}}{\partial r}\bigg|_{r=R_s} - \frac{u_s^{de}(x, R_s, t)}{R_s^2} = -\frac{}{D_s} \quad [31]$$

Ion diffusion in the electrolyte.—Under the approximation of fast relaxation of the double layer, the movement of Li ions in the electrolyte that is pervasive throughout the electrode is described in a slightly more generalised form than the "traditional" single particle model with electrolyte,[53] since the equilibrium reactivity $j(\eta^*(x))$ is allowed to vary in space, according to

$$\varepsilon(x)\frac{\partial c_e(x, t)}{\partial t} = \frac{\partial}{\partial x}\left(D_e^{eff}(x)\frac{\partial c_e(x, t)}{\partial x}\right)$$
$$+ \frac{(1 - t_+)}{F}j(\eta^*(x)) \quad [32]$$

in the graded cathode and

$$\varepsilon\frac{\partial c_e(x, t)}{\partial t} = D_e^{sep}\frac{\partial^2 c_e(x, t)}{\partial x^2} \quad [33]$$

in the separator, subject to the boundary conditions

$$\frac{\partial c_e(x, t)}{\partial x}\bigg|_{x=0} = \frac{\partial c_e(x, t)}{\partial x}\bigg|_{x=L+L_s} = 0, \quad [34]$$

$$D_e^{eff}\frac{\partial c_e(x, t)}{\partial x}\bigg|_{x=L} = D_e^{sep}\frac{\partial c_e(x, t)}{\partial x}\bigg|_{x=L} = 0. \quad [35]$$

The contribution to the voltage[53] is

$$v_{ce}(t) = \frac{2RT(1 - t_+)}{F}(\ln(c_e(L, t)) - \ln(c_e(0, t)), \quad [36]$$

$$\approx \frac{2RT(1 - t_+)}{Fc_e^*}(c_e(L, t) - c_e(0, t)) \quad [37]$$

under the small signal assumption of impedance analysis that the electrolyte concentration remains near equilibrium $c_e \approx c_e^*$.

Contact resistance.—The electrochemical effects described above are typically sufficient to describe the impedance response of many battery chemistries. However, for LFP half-cells, two additional effects need to be included:[46] a contact resistance at the current collector interface and ion movement through the SEI layer encapsulating the particles.

At frequencies $\omega \approx 10^5$ Hz, the contact resistance at the interface between the current collector and the cathode dominates the impedance response.[46,60,62] Here, this effect is described by a first order relaxation

$$\dot{\phi}_{con}(t) = -\frac{1}{R_{con}C_{con}}\phi_{con}(t) + \frac{i(t)}{C_{con}}, \qquad [38]$$

$$v_{contact}(t) = \phi_{con}(t). \qquad [39]$$

SEI Layer at the Li-foil Anode.—Ion movement through the SEI layer at the Li foil anode has also been identified (through inspecting activation energies[46]) as contributing to the impedance of LFP half-cells at frequencies $\omega \approx 10^3$ Hz.[46,63] Here, these fast dynamics are described by

$$\dot{\phi}_{SEI}(t) = -\frac{1}{R_{SEI}C_{SEI}}\phi_{SEI}(t) + \frac{i(t)}{C_{SEI}}, \qquad [40]$$

$$\dot{\phi}_{Li}(t) = \frac{i(t)}{C_{an}}, \qquad [41]$$

$$v_{anode}(t) = \phi_{SEI}(t) + \phi_{Li}(t). \qquad [42]$$

where ϕ_{SEI} captures the potential drop across the anode SEI layer and ϕ_{Li} accounts for the movement of Li from the foil to the cathode. The parameters $R_{SEI}C_{SEI}$ relate to the fast relaxation time constant at the SEI layer and C_{an} describes the buildup of Li moving from the foil to the cathode.

Constructing the Impedance Function

The model developed in the above section is now used to generate an impedance function for the Li-ion half-cells with graded LFP-based cathodes and lithium foil anodes. The impedance function was generated by spatially discretising the PDEs of the model Eqs. using the Chebyshev spectral collocation method[64] and linearising each term of the voltage expression in Eq. 14 before applying the Laplace transform to compute the gains from the current density to the voltage in Eq. 14 in the frequency range $10^{-2} \leqslant \omega \leqslant 10^6$ Hz. The impedance generated by the model can be decomposed into predominant contributions under different conditions, e.g. due to the overpotential $G_\eta(s)$ (described in the "Overpotential dynamics" section), related to the charge transfer

resistance which was apparent when $\omega \approx 10^2$ Hz; the particles $G_{c_s^{surf}}(s)$ (described in the "Ion diffusion in the active materials" section), which was the dominant process at low frequencies $\omega < 10^{-1}$ Hz; the bulk transport effect $G_{c_e}(s)$ (described in the "Ion diffusion in the electrolyte" section) which was found to be negligible; the anode $G_{an}(s)$ (described in the "SEI Layer at the Li-foil anode" section), which also operated at $\omega \approx 10^3$ Hz; and the high-frequency contact resistance $G_{con}(s)$ (described in the "Contact resistance" section) active at high frequencies of $\omega \approx 10^5$. The total impedance $G(s)$ is then the sum of each of these contributions

$$G(s) = G_\eta(s) + G_{c_s^{surf}}(s) + G_{c_e}(s)$$
$$+ G_{an}(s) + G_{con}(s) + R_{res}. \qquad [43]$$

Results

The simulated and experimental[15] impedance responses of the uniform, CAC@ and AC@ electrodes, with the same overall thicknesses and fraction of active material are shown in Figs. 3 (Nyquist plots) and 5 (Bode plots), using the model parameters shown in Table II and III. The physical interpretation of the impedance plots can be used to understand the role of electrode grading on LFP cathodes, for which more accurate than review in Ref. 46 is discussed next.

In the Nyquist plots in Fig. 3, there was generally a good fit between the simulated impedance response and the experimental data, with the model able to capture and differentiate the responses of the CAC@, AC@ and uniform electrodes with a similar level of discrimination as experiment. The reduced charge transfer and SEI resistances of the graded electrodes (a consequence of the heterogeneous structures exploiting changes in local electrical conductivity) were readily apparent and explain the increased capacity of graded electrodes (105 mAhg^{-1} at 1C[16]) over uniform electrodes (48 mAhg^{-1} at 1C[16]), and at higher C-rates (>1C).[15] These reduced resistances confirmed that an increased carbon content at the current collector, as adopted in the AC@ and CAC@ electrode structures, was critical to improving LFP-based cathode performance. One insight of this finding may be that if carbon coating of LFP particles is to be used (as is commonly the case),[65] it would be most effectively applied to those particles close to the current collector and may be less beneficial elsewhere. It is also noted that the observed reductions in $G_{an}(s)$ at high frequencies of the graded electrodes could be due to their increased carbon content reducing the contact resistance at the cathode/current collector interface- with this effect being incorporated within $G_{an}(s)$.
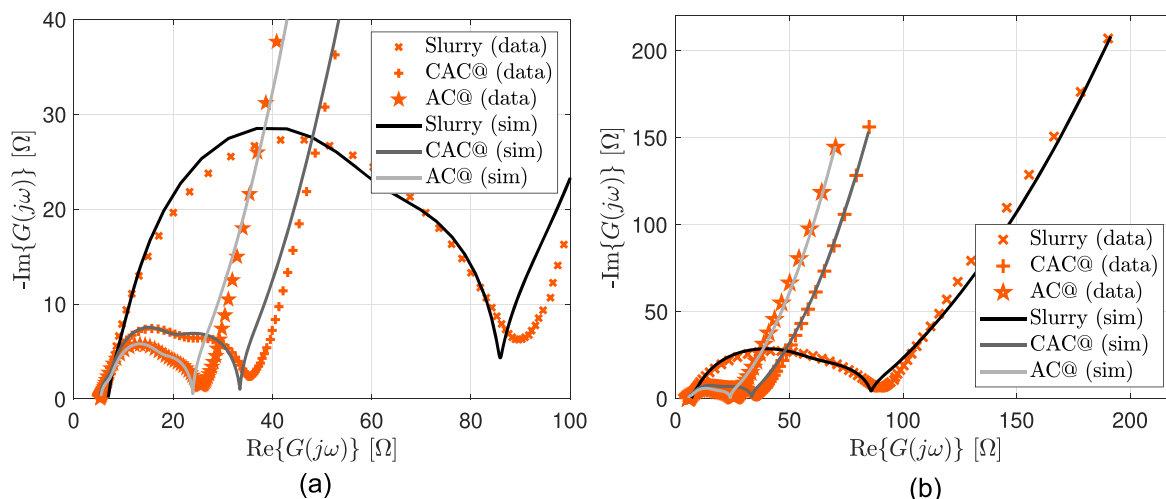
Figure 3. Nyquist plots of spray printed graded CAC@ and AC@ electrodes, and slurry cast uniform electrodes in a half-cell configuration, by simulation and the corresponding experimental data from Ref. 15. (a) Simulated electrode impedance response and corresponding experimental data at high frequency. (b) Simulated electrode impedance response and corresponding experimental data.
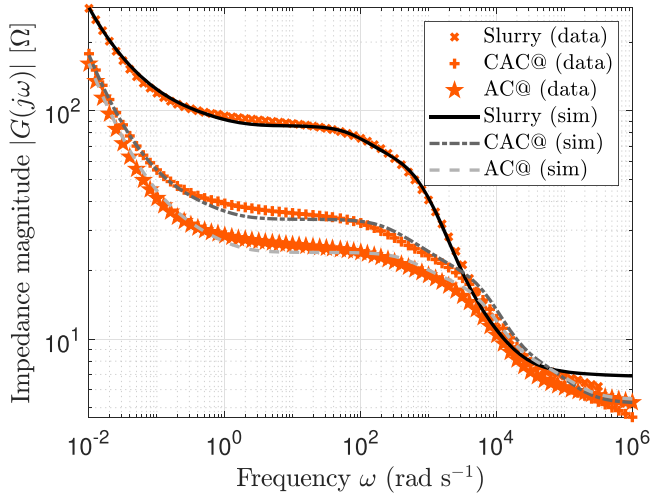
Figure 4. Bode plot showing the simulated magnitude of the impedance response $|G(j\omega)|$ for each electrode design, and the corresponding experimental data.

The Bode plot in Fig. 4 provides information on the pole locations of the electrochemical system ("poles" referring to its use in control theory, and being the negative of the reciprocal of a time constant). At comparatively low frequencies $\omega < 10^{-1}$ Hz, relatively slow ion diffusion in the active (LFP) particles dominated the cathode response; at $\omega \approx 10^2$ Hz there was a pole attributed to the charge transfer resistance; at $\omega = 10^3$ Hz there was a further pole normally ascribed to the SEI interface, and at $\omega \approx 10^5$ Hz there was a pole from the contact resistance. Figure 4 suggests that the effect of electrode grading was primarily to increase the effective conductivity, resulting in a lower impedance. It should be noted that the overall carbon content of all the electrodes was identical, and that these relatively strong effects were due principally to locating the carbon in regions where its conducting function was maximised.

One of the key objectives of electrochemical battery modelling is to use simulations to disentangle the contributions of the various and complex inter-related physical phenomena. For example, the set of Bode plots in Figs. 5a to c for AC@, CAC@ and the uniform electrodes respectively show the magnitudes of the impedance components for each cell configuration, and how grading can reduce the charge transfer and SEI resistances of the cell, consistent with experiment.[15]

Considering the implications of the impedance results and a desire to rationalise the behavior into a more general form, we now consider the implications of the ratio of electronic conductivity at the current collector to ionic conductivity at the separator, $\sigma(0)/\kappa(L)$, and its role in the behavior of graded electrodes. But first, let us consider the case of a simpler uniform microstructure electrode where the equilibrium overpotential satisfies

$$\frac{\partial^2 \eta^*(x)}{\partial^2 x} - \omega^2 \eta^*(x) = 0,$$

$$\text{with} \quad \omega^2 = \left(\frac{1}{\sigma} + \frac{1}{\kappa}\right)\left(\frac{a_s}{r_{SEI} + \frac{RT}{i_0}}\right), \qquad [44]$$

and is subject to the boundary conditions of Eqs. 20–21. The solution to this equation is

$$\eta^*(x) = (A_\eta e^{\omega x} + B_\eta e^{\omega(x-L)})i(t), \qquad [45]$$

where

$$B_\eta = \frac{\left(\frac{1}{\sigma \omega} + \frac{e^{-\omega L}}{\kappa \omega}\right)}{(e^{\omega L} - e^{-\omega L})}, \quad A_\eta = B e^{\omega L} - \frac{1}{\sigma \omega}, \qquad [46]$$

as plotted in Fig. 6. A quadratic approximation of $\eta^*(x)$ to simplify this overpotential distribution uses a Taylor expansion for relatively thin electrodes

$$\eta^*(x) \approx \eta^*_{quad}(x) = e_0 + e_1 x + e_2 x^2. \qquad [47]$$

Matching up the boundary conditions and setting e_0 to minimize the integral of Eq. 44 gives

$$e_0 = \left(\left(\frac{r_{SEI} + \frac{RT}{i_0}}{a_s L}\right) + \frac{L}{3\sigma} - \frac{L}{6\kappa}\right)i(t),$$

$$e_1 = -\frac{i(t)}{\sigma},$$

$$e_2 = \left(\frac{1}{\sigma} + \frac{1}{\kappa}\right)\frac{i(t)}{2L}.$$

This simplified solution $\eta^*_{quad}(x)$ is also plotted in Fig. 6 and shows a good approximation to the analytic solution $\eta^*(x)$.

The position through the uniform electrode thickness with the lowest overpotential is given by

$$x^* = \left(\frac{1}{1 + \frac{\sigma}{\kappa}}\right)L, \qquad [48]$$

which is obtained by solving $d\,\eta^*_{quad}(x)/dx = 0$. As the quadratic $\eta^*_{quad}(x)$ is an even function taking its maximum value at the electrode edge furthest away from x^*, the importance of the $\frac{\sigma}{\kappa}$ ratio in determining the location of peak $\eta^*(x)$, and hence peak reactivity from the Butler-Volmer kinetics of Eq. 13, is apparent from Eq. 48. Specifically, at x^* the minimum overpotential is obtained

$$\underline{\eta}^*(x) = \min \eta^*_{quad}(x) = \eta^*_{quad}(x^*) = \left(\left(\frac{r_{SEI} + \frac{RT}{i_0}}{a_s L}\right)\right.$$

$$\left. + \frac{L}{3\sigma} - \frac{L}{6\kappa} - \frac{L}{2\sigma\left(1 + \frac{\sigma}{\kappa}\right)}\right)i(t),$$

with the maximum found at an electrode interface, depending upon the $\frac{\sigma}{\kappa}$ ratio,

$$\bar{\eta}^*(x) = \max \eta^*_{quad}(x)$$

$$= \begin{cases} \eta^*_{quad}(0) = \left(\left(\frac{r_{SEI} + \frac{RT}{i_0}}{a_s L}\right) + \frac{L}{3\sigma} - \frac{L}{6\kappa}\right)i(t), & \text{if } \frac{\sigma}{\kappa} \leqslant 1, \\ \eta^*_{quad}(L) = \left(\left(\frac{r_{SEI} + \frac{RT}{i_0}}{a_s L}\right) - \frac{L}{6\sigma} + \frac{L}{3\kappa}\right)i(t), & \text{if } \frac{\sigma}{\kappa} > 1. \end{cases}$$

From these expressions, the variation of the overpotential through the electrode is

$$\Delta\eta^* = \bar{\eta}^*(x) - \underline{\eta}^*(x) = \begin{cases} \dfrac{LI(t)}{2S_A \sigma\left(1 + \frac{\sigma}{\kappa}\right)}, & \text{if } \frac{\sigma}{\kappa} \leqslant 1, \\ \dfrac{LI(t)}{2S_A}\left(\frac{1}{\kappa} - \frac{1}{\sigma} + \frac{\frac{\sigma}{\kappa}}{\kappa(1 + \frac{\sigma}{\kappa})}\right), & \text{if } \frac{\sigma}{\kappa} > 1. \end{cases}$$
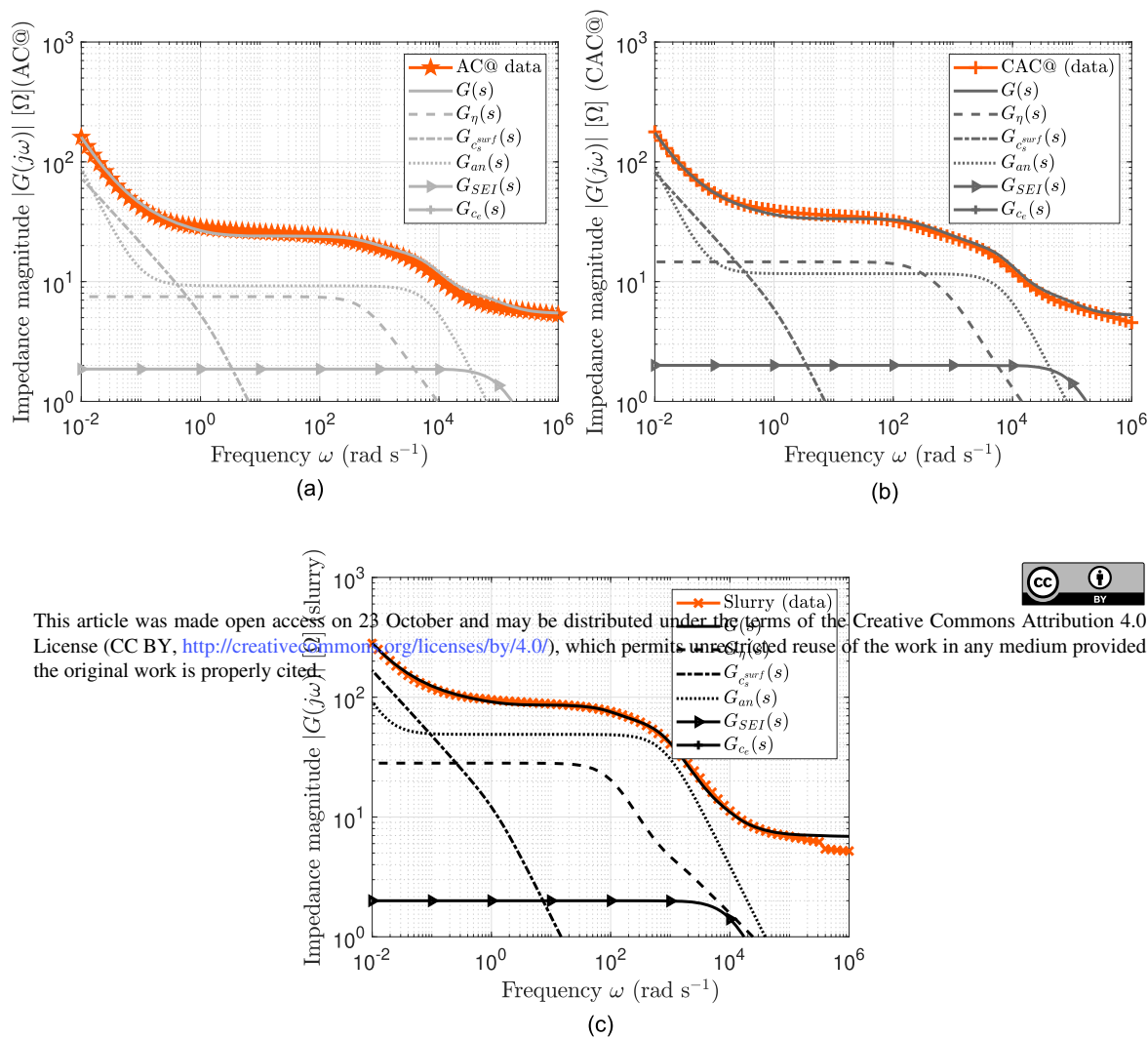
Figure 5. Magnitude of each component of the impedance response for CAC@, AC@ and uniform electrodes. Contact resistance reduction was the main reason for the lower resistance of the graded half-cells. The simulated impedance is decomposed into terms from the charge transfer resistance $G_\eta(s)$, diffusion in the solid particles $G_{c_s^{surf}}(s)$, the electrolyte $G_{c_e}(s)$ (negligible in this case), the anode $G_{an}(s)$ and the contact resistance $G_{con}(s)$. (a) The simulated impedance components that form the impedance response of the AC@ graded electrode, and experimental data. (b) The simulated impedance components that form the impedance response of the CAC@ graded electrode, and experimental data. (c) The simulated impedance components that form the impedance response of the uniform electrode, and experimental data.

Notice that if $\sigma/\kappa \ll 1$ then the overpotential variation tends to $\Delta\eta^* \approx L/(2S_A\sigma)$ but if $\sigma/\kappa \gg 1$ then $\Delta\eta^* \approx L/(2S_A\kappa)$, with these expressions connecting the overpotential drop across an electrode (reflecting the variation of its reaction kinetics) to the cell dimensions and dominant electronic or ionic conductivity. This analysis implies that for uniform or slightly graded electrodes, the $\sigma(0)/\kappa(L)$ ratio will play a key role in determining the position of maximum reactivity, with the Butler-Volmer kinetics of Eq. 11 linking the local overpotential to local reactivity.

As the overpotential drives the interfacial reaction rate $j(\eta(x, t))$, then if $\sigma(0) \ll \kappa(L)$, as is typically the case for LFP cells with $\sigma \approx 10^{-1}$ S m^{-1}[116] and $\kappa \approx 1$ S m^{-1}[66] the peak reactivity will be at the current collector. But, if $\sigma(0) \gg \kappa(L)$, as is the case for LIB cathode materials such as LiNi$_{1-x-y}$Mn$_x$Co$_y$O$_2$ (NMC) where $\sigma \approx 10^1$ S m^{-1},[67] and $\kappa \approx 1$ S m^{-1},[43] the active particles at the separator will experience the peak reactivity. Particles in the region of peak initial reactivity will discharge first—following Eq. 31—and so, for large enough current densities these particles will be cycled most fully and fastest. Since charge/discharge almost always involves particle volume change, and thus potentially pulverising strains, active particles in this relatively reactive local region will tend to experience the highest strains and likelihood of fracture,

isolation and resulting in a progressive loss of capacity. Thus, we can now see that a reason for grading is to move a proportion of active particles away from this highly active region (and replacing them with another material). Grading optimisation therefore involves deciding how much active material can be moved, and where, before overall capacity is reduced. The optimum will lie in an arrangement where the most uniform electrochemical response of the electrode as a whole combines with the smallest impedance, i.e. the flattest and lowest curve in Fig. 7, increasing the overall realisable and useful cycle life.

Returning to the specific case of the graded LFP cells studied here, since $\sigma(0) \ll \kappa(L)$, the implication is that a proportion of active particles should be moved away from the comparatively reactive current collector region to improve overall electrode response, and was consistent with the improved performance of the AC@ and CAC@ designs (and the poorer performance of the CA@ design) in Ref. 15). Reinforcing this notion, Fig. 7 plots the overpotential distributions for both the graded AC@, CAC@ and uniform electrodes obtained by solving Eq. 22. The overpotential of both graded electrodes were lower than the equivalent uniform electrode (and the AC@ design notably flatter), supporting that heterogeneous electrode structures can homogenise and reduce overpotential
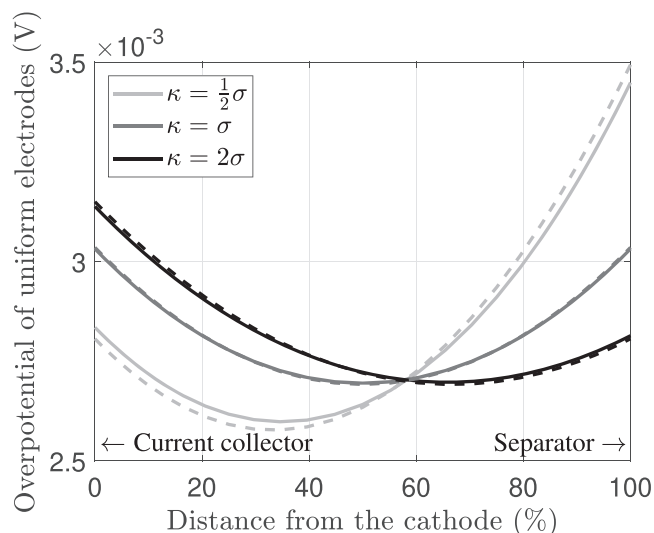
Figure 6. Overpotential distribution through the thickness of a uniform electrode with various σ/κ ratios and a unit applied current $I(t) = 1$A. When $\sigma/\kappa < 1$, peak reactivity is at the current collector but when $\sigma/\kappa > 1$ it is at the separator. This indicates the reaction to occur more regularly distributed from these highly reactive regions. The dashed lines correspond to the approximated quadratic solution of Eq. 5.
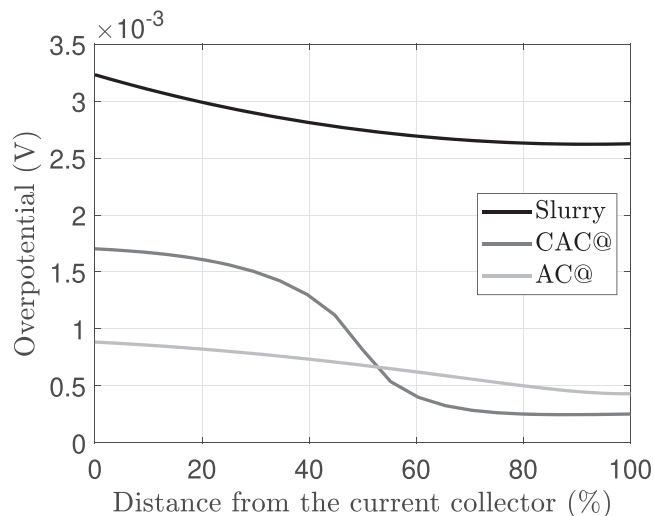
Figure 7. Comparison of the through-thickness overpotential distributions for both the graded and uniform slurry cast electrodes with a unit applied current $I(t) = 1$ A. The reduced overpotentials of the graded electrodes imply they can more effectively exploit the fixed overall fraction of carbon conducting additive.

distributions by reducing electrode resistance and avoiding excessive, local pulverisation of active material.

By extension, for cathodes based on NMC for example, it is expected that performance benefits might be provided if the configuration were reversed, and the separator region was carbon rich. Thus, there is no "universal" best arrangement of the various particulates in a Li-ion battery electrode, but for each cathode chemistry an optimum arrangement (for a fixed fraction of each component) may exist, which will depend on the ionic and electronic conductivity behavior of the electrode materials, and how their spatial distribution is contrived. Indeed, for some electrode compositions, the optimum arrangement may be acceptably close to a uniform distribution of constituents (at least for relatively thin electrodes and at modest C-rate), as is produced to such great effect at scale by slurry casting. However, for some chemistries and fixed

fractions of materials, or if ultra-thick and/or high-power electrodes are required, the optimum arrangement may be a graded or layered arrangement, the details of which can be guided by models of the type described here. Such work for NMC and other compositions is currently underway.

Recalling Fig. 1 and the variations in local porosity fraction that are an inevitable consequence of changing the local composition, it should be considered to what extent porosity variations might be responsible for the observed trends. This aspect is yet to be addressed in detail by simulations. However, it should be noted that a series of uniform electrodes with varying composition and porosity were produced to obtain the data in Fig. 1 and electrochemically tested.[15] None of these electrodes performed as well as the CAC@ graded electrode, supporting the notion that while porosity changes will contribute to differing electrode dynamics, for the materials and ranges studied here, they were a second order effect that could be captured in the model through changes in the electrical resistance.

Conclusions

An electrochemical model has been developed and explored to improve understanding of electrode composition grading at the microstructural scale on the performance of Li-ion batteries. The graded electrodes—or hetero-electrodes—have controlled variations in the local proportion of electrode constituent materials: active, carbon and binder. The model incorporated these spatial variations explicitly, including local porosity changes, and showed a high level of agreement with experimental impedance data for the case of Li-ion half cells using LiFePO$_4$(LFP)-based cathodes.

The model was then used to explain the experimental behavior of graded electrodes. First, it was shown that increasing the carbon content at the current collector/cathode interface led to a significant reduction in the charge transfer and SEI resistances in the impedance response. Second, it was shown that, compared with uniform microstructure electrodes, graded electrodes can reduce the overpotential distribution through the electrode thickness, which in turn gave rise to qualitative ideas and guidelines for the design of optimised graded electrodes. In particular, for LFP electrodes, it was shown that since ionic conductivity dominated over electronic conductivity, the initial (most reactive) region of discharge of the cathode was at the current collector/cathode interface, and so, for high C-rates, particles in this region experienced the highest amount of usage (and therefore induced intercalation strain), were more likely to be pulverised. To limit the fraction of highly strained active particles, a proportion of particles should be moved away from this region to extend their lifetime and ongoing contribution to overall capacity, and an optimum local fraction will exist. The reverse arrangement should hold for cells where the electronic conductivity is significantly higher than the ionic conductivity. With an understanding of the benefits of grading on LFP electrodes now generalised, an approach on how to design graded electrodes to facilitate better batteries can be conjectured; conditions where grading may or may not be useful can now be better identified.

More simply, the same approach (and model) can be used to identify the optimum fraction of constituent materials in electrode where grading is unavailable—as is currently the case for the vast majority of electrodes. For some required performance characteristics, the optimum distribution may sit in a broad and flat part of composition space where small changes make little difference; for others, for example, as thickness is increased or more power is sought, the optimum uniform composition may change. Indeed, practical experience shows for some electrodes, more carbon or more carefully distributed carbon, is needed to produce the required performance. The model and insights described here suggest that this optimisation is in effect, attempting to homogenize the overpotential and reactivity distribution. In many cases, this can be achieved acceptably with a uniform composition, in other cases; grading can produce significant benefits.

ORCID

R. Drummond https://orcid.org/0000-0002-2586-1718

References

1. B. Nykvist and M. Nilsson, *Nature Climate Change*, **5**, 329 (2015).
2. Y. Wang, X. Fu, M. Zheng, W. H. Zhong, and G. Cao, *Adv. Mater.*, **31**, 1804204 (2019).
3. M. M. Forouzan, B. A. Mazzeo, and D. R. Wheeler, *J. Electrochem. Soc.*, **165**, A2127 (2018).
4. S. Paul, C. Diegelmann, H. Kabza, and W. Tillmetz, *Journal of Power Sources*, **239**, 642 (2013).
5. F. M. Kindermann, P. J. Osswald, G. Ehlert, J. Schuster, A. Rheinfeld, and A. Jossen, *J. Electrochem. Soc.*, **164**, E3105 (2017).
6. B. Wu, V. Yufit, M. Marinescu, G. J. Offer, R. F. Martinez-Botas, and N. P. Brandon, *Journal of Power Sources*, **243**, 544 (2013).
7. K. Song, C. Zhang, N. Hu, X. Wu, and L. Zhang, *Electrochimica Acta*, **377**, 138105 (2021).
8. R. Rodriguez, L. J. Deiner, B. H. Tsao, and J. P. Fellner, *ACS Appl. Energy Mater.*, **4**, 9507 (2021).
9. C. Huang, N. P. Young, J. Zhang, H. J. Snaith, and P. S. Grant, *Nano Energy*, **31**, 377 (2017).
10. C. Huang, N. P. Young, J. Zhang, H. J. Snaith, and P. S. Grant, *Nano energy*, **31**, 377 (2017).
11. S. Kalnaus, Kidanu Abay, J. Hawley, H. Wang, and J. Li, *Journal of Energy Storage*, **44**, 103582 (2021).
12. R. Drummond, C. Huang, P. Grant, and S. Duncan, *Journal of Power Sources*, **433**, 126579 (2019).
13. J. W. Palko, A. Hemmatifar, and J. G. Santiago, *Journal of Power Sources*, **397**, 252 (2018).
14. C. Huang, J. Zhang, N. P. Young, H. J. Snaith, and P. S. Grant, *Sci. Rep.*, **6**, 25684 (2016).
15. C. Cheng, R. Drummond, S. R. Duncan, and P. S. Grant, *Journal of Power Sources*, **413**, 59 (2019).
16. C. Cheng, R. Drummond, S. R. Duncan, and P. S. Grant, *Journal of Power Sources*, **448**, 227376 (2020).
17. D. Westhoff et al., *Materials Characterization*, **151**, 166 (2019).
18. L. Liu, P. Guan, and C. Liu, *J. Electrochem. Soc.*, **164**, A3163 (2017).
19. T. F. Fuller, M. Doyle, and J. Newman, *J. Electrochem. Soc.*, **141**, 1 (1994).
20. S. Golmon, K. Maute, and M. L. Dunn, *Journal of Power Sources*, **253**, 239 (2014).
21. I. D. Campbell, K. Gopalakrishnan, M. Marinescu, M. Torchio, G. J. Offer, and D. Raimondo, *Journal of Energy Storage*, **22**, 228 (2019).
22. S. De, P. W. C. Northrop, V. Ramadesigan, and V. R. Subramanian, *Journal of Power Sources*, **227**, 161 (2013).
23. V. Ramadesigan, R. N. Methekar, F. Latinwo, R. D. Braatz, and V. R. Subramanian, *J. Electrochem. Soc.*, **157**, A1328 (2010).
24. Y. Dai and V. Srinivasan, *J. Electrochem. Soc.*, **163**, A406 (2016).
25. Y. Qi, T. Jang, V. Ramadesigan, D. T. Schwartz, and V. R. Subramanian, *J. Electrochem. Soc.*, **164**, A3196 (2017).
26. S. T. Taleghani, B. Marcos, K. Zaghib, and G. Lantagne, *J. Electrochem. Soc.*, **166**, A225 (2019).
27. S. T. Taleghani, B. Marcos, K. Zaghib, and G. Lantagne, *J. Electrochem. Soc.*, **164**, E3179 (2017).
28. R. Fang, H. Ge, Z. Wang, Z. Li, and J. Zhang, *J. Electrochem. Soc.*, **167**, 130513 (2020).
29. B. Suthar, P. W. C. Northrop, D. Rife, and V. R. Subramanian, *J. Electrochem. Soc.*, **162**, A1708 (2015).
30. V. Srinivasan and J. Newman, *J. Electrochem. Soc.*, **151**, A1530 (2004).
31. T. F. Fuller, M. Doyle, and J. Newman, *J. Electrochem. Soc.*, **141**, 1 (1994).
32. J. Haverkort, *Electrochimica Acta*, **295**, 846 (2019).
33. R. Drummond, S. Zhao, and S. R. Duncan, *IEEE Transactions on Control Systems Technology*, **27**, 1071 (2018).
34. N. Nitta, F. Wu, J. T. Lee, and G. Yushin, *Mater. Today*, **18**, 252 (2015).
35. S. Dühnen, J. Betz, M. Kolek, R. Schmuch, M. Winter, and T. Placke, *Small Methods*, **4**, 2000039 (2020).
36. J. Wang, P. Liu, J. Hicks-Garner, E. Sherman, S. Soukiazian, M. Verbrugge, H. Tataria, J. Musser, and P. Finamore, *Journal of Power Sources*, **196**, 3942 (2011).
37. K. Striebel, J. Shim, V. Srinivasan, and J. Newman, *J. Electrochem. Soc.*, **152**, A664 (2005).
38. Y. Tang, M. Jia, J. Li, Y. Lai, Y. Cheng, and Y. Liu, *J. Electrochem. Soc.*, **161**, E3021 (2014).
39. M. Wang, J. Li, X. He, H. Wu, and C. Wan, *Journal of Power Sources*, **207**, 127 (2012).
40. A. Masliy and N. Poddubny, *Journal of Applied Electrochemistry*, **27**, 1036 (1997).
41. A. Masliy and N. Poddubny, *Journal of Applied Electrochemistry*, **27**, 1045 (1997).
42. A. Masliy and N. Poddubny, *Journal of Applied Electrochemistry*, **28**, 589 (1998).
43. Y. Yang et al., *Adv. Energy Mater.*, **9**, 1900674 (2019).
44. V. Srinivasan and J. Newman, *J. Electrochem. Soc.*, **151**, A1517 (2004).
45. V. Srinivasan and J. Newman, *Electrochem. Solid-State Lett.*, **9**, A110 (2006).
46. J. P. Schmidt, T. Chrobak, M. Ender, J. Illig, D. Klotz, and E. Ivers-Tiffée, *Journal of Power Sources*, **196**, 5342 (2011).
47. M. Gaberšček, *Nat. Commun.*, **12**, 1 (2021).
48. M. Doyle, T. Fuller, and J. Newman, *J. Electrochem.*, 26 (1993).
49. J. Newman and W. Tiedemann, *AIChE J.*, **21**, 25 (1975).
50. J. Newman, *Electrochemical systems*, NDL, New Jersey, (2012).
51. H. Zheng, R. Yang, G. Liu, X. Song, and V. S. Battaglia, *The Journal of Physical Chemistry C*, **116**, 4875 (2012).
52. H. Kondo, H. Sawada, C. Okuda, and T. Sasaki, *J. Electrochem. Soc.*, **166**, A1285 (2019).
53. S. J. Moura, F. B. Argomedo, R. Klein, A. Mirtabatabaei, and M. Krstic, *IEEE Transactions on Control Systems Technology*, **25**, 453 (2016).
54. X. Lin, J. Park, L. Liu, Y. Lee, A. Sastry, and W. Lu, *J. Electrochem. Soc.*, **160**, A1701 (2013).
55. L. Liu, J. Park, X. Lin, A. M. Sastry, and W. Lu, *Journal of power sources*, **268**, 482 (2014).
56. L. Liu and M. Zhu, *ECS Trans.*, **61**, 43 (2014).
57. A. M. Bizeray, S. Zhao, S. R. Duncan, and D. A. Howey, *Journal of Power Sources*, **296**, 400 (2015).
58. I. J. Ong and J. Newman, *J. Electrochem. Soc.*, **146**, 4360 (1999).
59. R. Drummond, A. Bizeray, D. Howey, and S. R. Duncan, *IEEE Transactions on Control Systems Technology*, **28**, 1284 (2019).
60. M. Gaberscek, J. Moskon, B. Erjavec, R. Dominko, and J. Jamnik, *Electrochem. Solid-State Lett.*, **11**, A170 (2008).
61. H. Matsui, T. Nakamura, Y. Kobayashi, M. Tabuchi, and Y. Yamada, *Journal of Power Sources*, **195**, 6879 (2010).
62. I. V. Thorat, T. Joshi, K. Zaghib, J. N. Harb, and D. R. Wheeler, *J. Electrochem. Soc.*, **158**, A1185 (2011).
63. A. Zaban, E. Zinigrad, and D. Aurbach, *The Journal of Physical Chemistry*, **100**, 3089 (1996).
64. L. N. Trefethen, *Spectral methods in MATLAB* (SIAM, Philadelphia, PA) 10 (2000).
65. H. C. Shin, W. I. Cho, and H. Jang, *Electrochimica Acta*, **52**, 1472 (2006).
66. J. Li, Y. Cheng, M. Jia, Y. Tang, Y. Lin, Z. Zhang, and Y. Liu, *Journal of Power Sources*, **255**, 130 (2014).
67. M. Ecker, S. Käbitz, I. Laresgoiti, and D. U. Sauer, *J. Electrochem. Soc.*, **162**, A1849 (2015).